The Planetary Science Journal, 4:105 (7pp), 2023 June https://doi.org/10.3847/PSJ/acd844
© 2023. The Author(s). Published by the American Astronomical Society.
OPEN ACCESS

Simulating Secondary Electron and Ion Emission from the Cassini Spacecraft in Saturn's Ionosphere

Z. Zhang[1], R. T. Desai[1,2], O. Shebanits[3], F. L. Johansson[4], Y. Miyake[5], and H. Usui[5]
[1] Blackett Laboratory, Imperial College London, UK; zeqi.zhang17@imperial.ac.uk
[2] Centre for Fusion, Space and Astrophysics, University of Warwick, UK
[3] Swedish Institute of Space Physics, Uppsala, Sweden
[4] ESA/ESTEC, Noordwijk, The Netherlands
[5] Graduate School of System Informatics, Kobe University, Kobe, Japan
Received 2022 September 5; revised 2023 May 14; accepted 2023 May 22; published 2023 June 13

Abstract

The Cassini spacecraft's Grand Finale flybys through Saturn's ionosphere provided unprecedented insight into the composition and dynamics of the gas giant's upper atmosphere and a novel and complex spacecraft–plasma interaction. In this article, we further study Cassini's interaction with Saturn's ionosphere using three-dimensional particle-in-cell simulations. We focus on how electrons and ions, emitted from spacecraft surfaces due to the high-velocity impact of atmospheric water molecules, could have affected the spacecraft potential and low-energy plasma measurements. The simulations show emitted electrons extend upstream along the magnetic field, and for sufficiently high emission rates, charge the spacecraft to positive potentials. The lack of accurate emission rates and characteristics, however, makes differentiation between the prominence of secondary electron emission and ionospheric charged dust populations, which induce similar charging effects, difficult for Cassini. These results provide further context for Cassini's final measurements and highlight the need for future laboratory studies to support high-velocity flyby missions through planetary and cometary ionospheres.

Unified Astronomy Thesaurus concepts: Planetary ionospheres (2185); Saturn (1426); Astrophysical dust processes (99); Planetary atmospheres (1244); Planetary rings (1254); Space plasmas (1544)

1. Introduction

Cassini's Grand Finale obtained the first ever in situ measurement of Saturn's ionosphere. Passing through on 22 orbits prior to its final plunge, the spacecraft provided unprecedented observations from inside Saturn's D-ring down to 1360 km altitude (Ip et al. 2016; Dougherty et al. 2018; Hsu et al. 2018; Lamy et al. 2018; Mitchell et al. 2018; Roussos et al. 2018; Wahlund et al. 2018; Waite et al. 2018; Cravens et al. 2019). Cassini's Plasma Spectrometer (Young et al. 2004) was, however, offline after 2012, and significant unknowns remain regarding charged ion and dust populations and their influence on the gas giant's ionosphere.

Saturn's inner rings are inherently unstable and were identified as raining onto the top of the gas giant's equatorial ionosphere (Northrop & Hill 1982; Connerney & Waite 1984). This was subsequently observed by Cassini in situ, where the spacecraft's Ion and Neutral Mass Spectrometer (INMS), Cosmic Dust Analyser (CDA) and Charge Energy Mass Spectrometer (CEMS) detected ring fragments consisting of water, silicates, and organics inflowing at estimated fluxes between 4800 and 45,0000 kg s^{-1} (Hsu et al. 2018; Mitchell et al. 2018; Waite et al. 2018). Cassini's high velocity limited the spectroscoptic plasma measurements to <5 u, and the composition of Saturn's ionosphere has thus been inferred from the available measurements. For example, Cassini's Radio and Plasma Wave Science (RPWS) antenna observed up to an order of magnitude more electrons than 1–4 u positive ions, and ion populations of > 4 u were therefore inferred to be present (Waite et al. 2018). Cassini's Langmuir Probe also simultaneously measured nearly an order of magnitude greater positive ion currents compared with electron currents (Wahlund et al. 2018; Hadid et al. 2019; Morooka et al. 2019), and these observations were thus interpreted as arising from increasingly abundant populations of negatively charged ions and dust with decreasing altitude (Morooka et al. 2019), in addition to the larger >4 u positive ions.

Cassini's Langmuir Probe measured the bulk plasma currents and therefore uniquely provides a measure of all ionospheric plasma constituents. As an integral measurement, however, the interpretation of this data set is nontrivial. Two distinct interpretations of the LP data thus exist within the literature. Morooka et al. (2019) first reported the apparent current discrepancies as arising from significant populations of charged dust, an interpretation that has formed the basis for sequential studies of Saturn's ionosphere (e.g., Wahlund et al. 2018; Hadid et al. 2019; Shebanits et al. 2020; Zhang et al. 2021a). Johansson et al. (2022), however, recently suggested that less dust is present and that the LP current imbalance is caused by secondary electrons and ions, emitted due to impacting gas molecules.

The two contrasting interpretations of the LP data have the commonality that they both identify Cassini as having charged to positive floating potentials. Zhang et al. (2021a) examined the role of charged dust in charging Cassini and showed that this could charge Cassini to positive potentials when the negatively charged ion/dust mass was significantly greater than that of the positive ions/dust and when the electrons constitute less than 10% of the total electron density. In this study, we evaluate the hypothesis that secondary electron emissions in Saturn's ionosphere might have induced a similar effect. Given the differing interpretation of the LP data, we focus on

Original content from this work may be used under the terms of the Creative Commons Attribution 4.0 licence. Any further distribution of this work must maintain attribution to the author(s) and the title of the work, journal citation and DOI.

evaluating the effect on the spacecraft potential to provide complementary understanding of the underlying system state. The dynamics of the spacecraft floating potential in these conditions are also relevant to low-energy plasma measurements obtained during further high-velocity flyby missions of planetary and cometary environments.

To study the effect of secondary electron and ion emission (SEE and SIE) for the Cassini spacecraft during the Grand Finale, we utilize three-dimensional particle-in-cell (PIC) simulations, as follows: Section 2 introduces the methods of the simulation and describes the input parameters. Section 3 analyzes and discusses the results of the simulations as well as the varying of key parameters. Section 4 then concludes by summarizing the results and discusses the implications for our understanding of the low-energy plasma measurements of the composition of Saturn's ionosphere.

2. Method

In this study, we utilize the three-dimensional PIC simulation code for ElectroMagnetic Spacecraft Environment Simulation (EMSES) developed for a self-consistent analysis of spacecraft–plasma interactions at electron scales (Miyake & Usui 2009). We embed a toy model of Cassini to scale within a predefined simulation domain. The three-dimensional electrostatic simulations are run in the spacecraft frame where the inflowing ionospheric plasma consists of drifting Maxwellian velocity distributions. Each species has mass and charge normalized to the proton scale with a real ion-to-electron mass ratio. The spacecraft is treated as a perfect conductor, and a detailed description of conductors and the numeric can be found in the previous work (Zhang et al. 2021a).

We model Cassini at a representative altitude of 2500 km during Rev 292, as in the previous study (Zhang et al. 2021a), but instead of including "dust" particles, we evaluate the hypothesis that SEE and SIE currents present a viable alternative to charged dust currents. To thus compare the effect of dust and secondary electron emissions accurately and independently, we use similar environment parameters as in our previous study where the dust was investigated, but replace the dust populations with secondary ion and electron emissions. We then scale our simulation parameters across multiple orders of magnitude to represent a larger range of Saturn's ionosphere, as explained below.

To test the hypothesis, we balance the electron populations to match the positive ion densities derived from the Langmuir Probe (Morooka et al. 2019) and introduce secondary electron and ion particles emitted from the spacecraft due to neutral–spacecraft collisions. The bulk current, $I_{\rm total}$, onto Cassini can therefore be broken down into the electron current, $I_{\rm electron}$, the ion current, $I_{\rm ion}$, and the secondary currents $I_{\rm SEE}$ and $I_{\rm SIE}$:

$$I_{\rm total} = I_{\rm electron} + I_{\rm ion^+} + I^e_{\rm SEE} - I^r_{\rm SEE} + I^e_{\rm SIE} - I^r_{\rm SIE}, \qquad (1)$$

where, importantly, $\mathrm{I}^e_{\rm SEE}$ and $\mathrm{I}^e_{\rm SIE}$ are the emitted electron and ion currents, respectively, and $\mathrm{I}^r_{\rm SEE}$ and $\mathrm{I}^r_{\rm SIE}$ represents those returning to impinge upon Cassini. The same density of electrons and positive ions with mass 1.35 u are introduced in the simulations, as inferred from Langmuir Probe observations of the effective positive charge carrier at this altitude (Morooka et al. 2019). Increasing the positive ion mass was also found to have only a small impact on the potential (Zhang et al. 2021a; Figure 5(a) therein). We also consider a cooler ionosphere of 370 K. This temperature change is motivated by ionospheric models (Moore et al. 2008, 2018; Yelle et al. 2018; Müller-Wodarg et al. 2019) indicating ionospheric temperatures lower than the electron temperature inferred from Cassini's Langmuir Probe (Morooka et al. 2019), which is suggested to have been affected by secondaries (Johansson et al. 2022). As shown in the subsequent results, the differing temperature choices of Zhang et al. (2021a) and this study do not affect the trends reported. This choice also results in a smaller electron Debye length than previously considered. This requires a smaller grid width of 5 cm with a total grid of 256^3, across a total simulation box size of 12.8 m^3.

The emitted SEE and SIE current densities are a function of the atmospheric neutral number density, n, elementary charge, e, the spacecraft velocity, $v_{\rm sc}$, the yield defined as the number of electrons ejected per incident neutral, γ, and the spacecraft's geometric cross section, A, as

$$I^e_{\rm SEE/SIE} = \sum_\alpha n_\alpha\, e\, v_{sc}\, \gamma_\alpha\, A, \qquad (2)$$

where α represents the neutral species of interest. Due to the lack of laboratory experiments of quantum yields from Cassini's surface materials, the inclusion of emission requires careful consideration, and as a result we utilize and vary yields associated with water ions.

Schmidt & Arends (1985) determined yields experimentally from water molecules incident on three materials relevant for Giotto's 70 km s^{-1} flyby velocity of Comet 1P/Halley. Here, we took the measured value of $\gamma = 0.15$ as our base value of the SEE impact yield in our study. At an altitude of 2500 km, these values correspond to $\approx 10\,\mu\mathrm{A\,m}^{-2}$. However, it is necessary to also vary this emission rate across a large range of values when applying this in the actual model, for two reasons. First, there are significant uncertainties in adopting this rate for Cassini's Kapton blankets (Lin & Stultz 1995) and its lower 35 km s^{-1} flyby velocity compared to Giotto's 70 km s^{-1} velocity that Schmidt & Arends (1985) did their experiment on. Second, the neutral density increases exponentially with decreasing altitude in Saturn's ionosphere (Yelle et al. 2018), and as the secondary emission is directly proportional to the neutral density, varying the emission yield therefore captures this natural variation in Cassini's interaction with Saturn's ionosphere (Moore et al. 2018; Müller-Wodarg et al. 2019). Therefore, by varying the emission yield, γ, across multiple orders of magnitude, we qualitatively recover a feature of the interaction between the Cassini spacecraft and Saturn's ionosphere that varies with altitude, from little to no neutral content at the topside ionosphere down to the densest part of Saturn's ionosphere sampled. The variation therefore also qualitatively captures a variation of altitudes. In this regard, the sensitivity of Cassini spacecraft potential to the emission density at different regimes, as we will see below, may also be of use for future high-velocity flyby missions of ionospheric environments.

The secondary ion emission is anticipated to be between 5 and 40 times lower than electron yields, and we therefore implement this to be 10% of the electron yields with an emitted ion temperature of 10 eV (Schmidt & Arends 1985). In our simulations, the electron and ion secondaries are emitted as a Maxwellian distribution. We adopt yields due to neutral water ion density of $n = 1.5 \times 10^4$ cm^{-3} from the model of Moore et al. (2018), due to the significant effect of these species on the

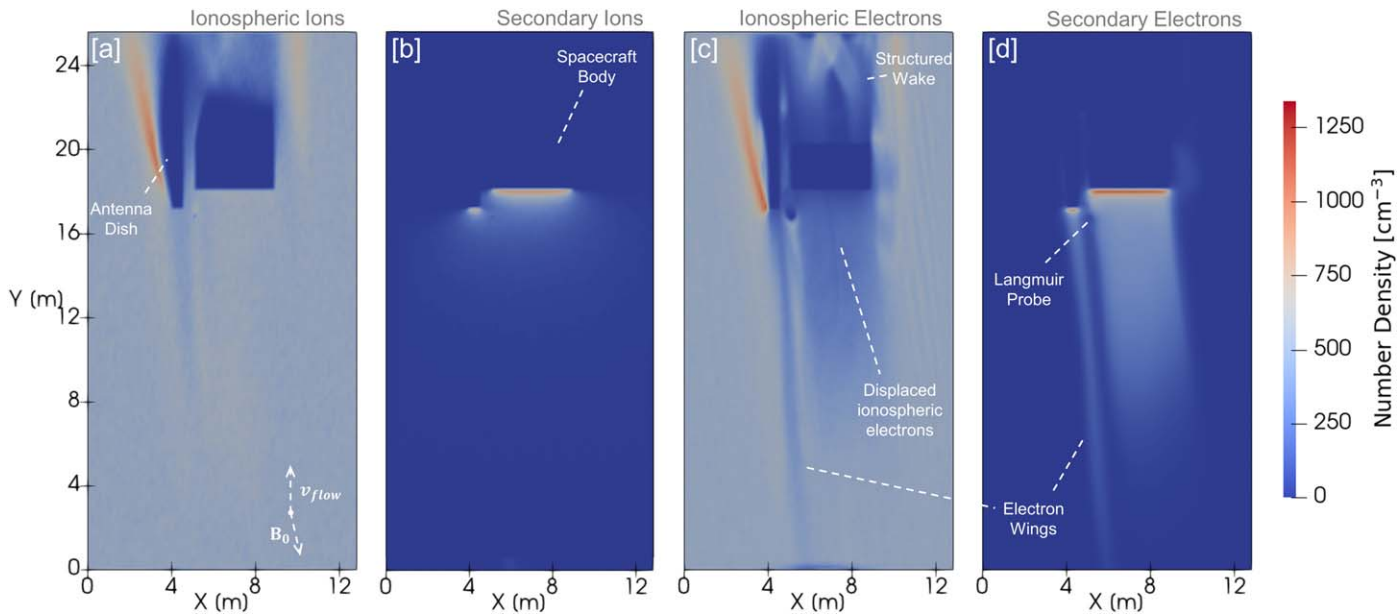

Figure 1. Simulated plasma densities around the Cassini spacecraft. (a) shows the ionospheric ions, (b) shows the secondary emitted ions, (c) shows the inospheric electrons, and (d) shows the secondary emitted electrons. The plasma velocity, $v_{\rm flow}$, is predominantly along the Y-axis, and the magnetic field, B_0, is approximately antiparallel to this. Specific input parameters can be found in Table 1. The ionospheric electrons are electrostatically displaced upstream, resulting in a combination of ionospheric and secondary electrons surrounding the spacecraft. Electrons wings caused by propagating Langmuir waves further modify the plasma ahead of the spacecraft, and the negatively biased Langmuir Probe is visible as a region devoid of plasma. A schematic of the simulated spacecraft geometry can be found in Figure 1 of Zhang et al. (2021a).

Giotto and Vega spacecraft, but as discussed previously, the variation in γ can be viewed as interchangeable with variations in n and therefore also altitude. Emissions from further species such as CH_4 and CO_2 might also contribute, given that kinetic electron emission processes (Sternglass 1957) will dominate over potential emission ones (Kishinevsky 1973) in this regime, but they are not included at this stage.

3. Results and Analysis

3.1. Plasma Interaction

Figure 1 shows the global plasma interaction between the Cassini spacecraft and Saturn's ionosphere at an altitude of 2500 km for the conditions outlined in Table 1. The color bar depicts the ion and electron densities (primary and secondary), the plasma is moving along the positive y-axis, and the magnetic field is approximately parallel to the y-axis. The spacecraft charges here to a positive potential.

A plasma wake can be clearly seen trailing behind the spacecraft at regions where the density is depleted. Due to the high speed of the plasma flows and nonzero potential of the spacecraft, the incoming ions and electrons are deflected around the sides of the spacecraft, forming enhanced densities adjacent to the wake. The probe swept from −4 to +4 V in Saturn's ionosphere and is negatively biased in this simulation, thus appearing as a region void of electrons. This biased potential also affects the surrounding plasma that subsequently impinges upon Cassini.

Secondary electrons and ions are generated at the surfaces of impact, simulating the incoming neutral impacts, and these result in electron and ion concentrations more than double the ambient ionospheric densities. These are generated in the spacecraft frame and are therefore able to diffuse away from the surfaces and upstream. This notably results in a decrease in the incoming ionospheric electron density ahead of the spacecraft.

Table 1
Environmental and System Simulation Parameters

Environmental Parameters	
Plasma ion density, n_0	505 cm^{-3}
Ion mass, m_i	1.35 amu
Electron temperature, T_e	0.031 8 eV (370 K)
Ion temperature, T_i	0.031 8 eV (370 K)
Magnetic field, $\boldsymbol{B}$	[1.48 $\hat{x}$, −14.8 $\hat{y}$, 1.24$\hat{z}$] μT
Flow velocity, $\boldsymbol{v}_{\rm flow}$	[−0.25 $\hat{x}$, −32.4 $\hat{y}$, −10.7 $\hat{z}$] km s^{-1}
Ion acoustic speed, v_S	2.47 km s^{-1}
Debye length, λ_D	5.90 cm
Electron gyroperiod, $\tau_{\rm ge}$	4.76 μs
Electron plasma period, $\tau_{\rm pe}$	4.98 μs
Ion gyroperiod, τ_{gi}	5.94 ms
Ion plasma period, τ_{pi}	0.247 ms
Electron emission density, $J_{\rm SEE}$	0.005–500 μA m^{-2}
Electron emission temperature, $T_{\rm SEE}$	2 eV
Ion emission density, $J_{\rm SIE}$	0.000 5–50 μA m^{-2}
Ion emission temperature, $T_{\rm SIE}$	10 eV
System Parameters	
Grid width, Δr	5 cm
Time step, Δt	0.033 μs
Simulation time, t	0.67 ms
Particles per cell	25

A unique aspect of this plasma regime is that the electron gyroradii are smaller than the spacecraft while the ion gyroradii are significantly larger. The emitted ions there appear to diffuse uniformly out in space upstream, whereas the electrons are tied to the field lines. This notably presents a prediction for when they might be detected, i.e., for a geometry where the Langmuir Probe is magnetically connected to Cassini's main body or antenna dish.

In front of the spacecraft, "electron wings" are present, formed by Langmuir waves propagating along the background

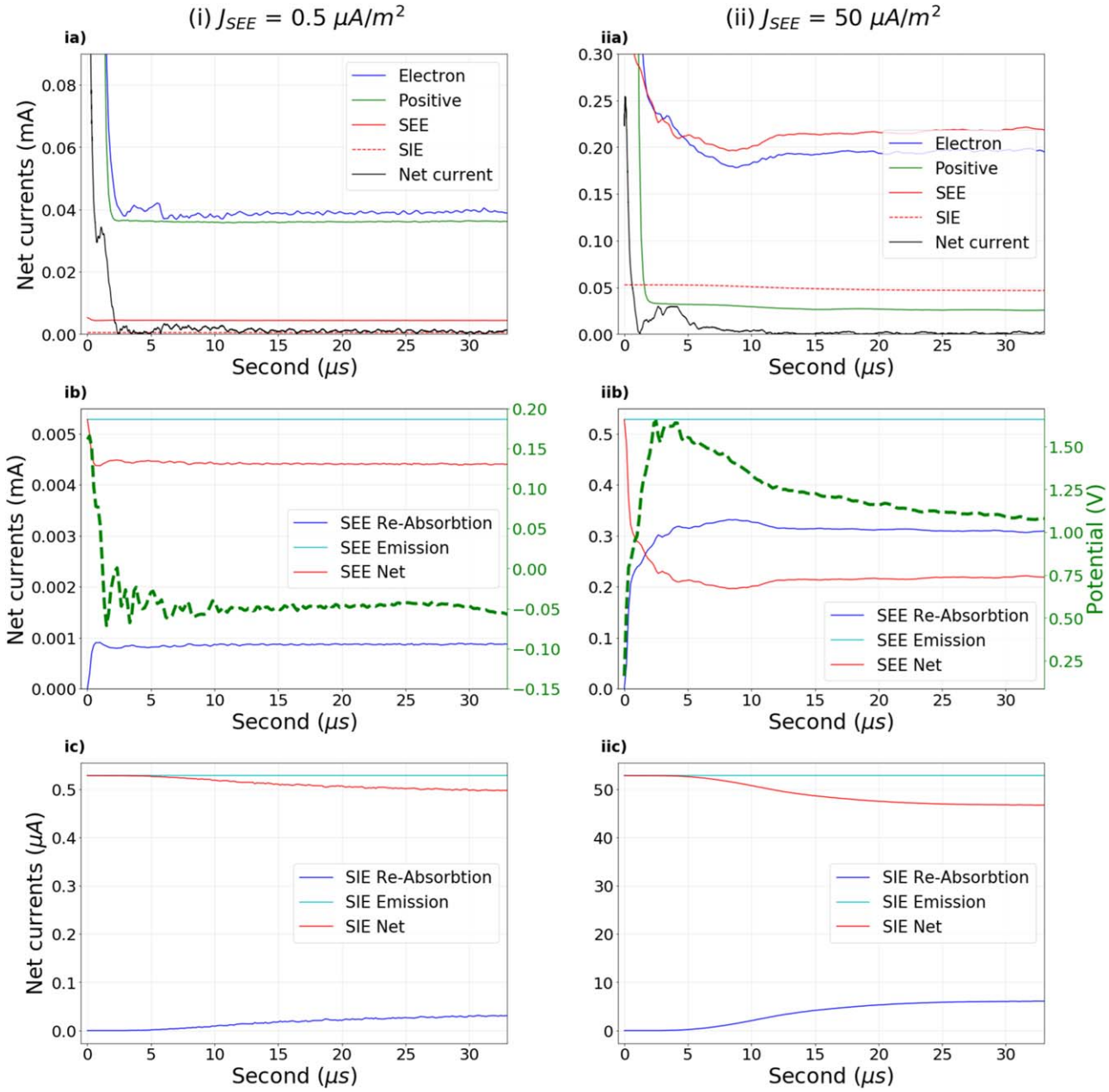

Figure 2. Currents onto the Cassini spacecraft's for two distinct regions: panels (ia–c) show the case of a negative floating potential induced when $I_{\rm SEE} = 0.5\ \mu{\rm A\ m}^{-2}$ and $I_{\rm SIE} = 0.05\ \mu{\rm A\ m}^{-2}$, and panels (iia–c) show the case of a positive floating potential induced when $I_{\rm SEE} = 50\ \mu{\rm A\ m}^{-2}$ and $I_{\rm SIE} = 0.5\ \mu{\rm A\ m}^{-2}$. The upper panels (ia) and (iia) show all the positive and negative currents inclusive, panels (ib) and (iib) show the currents associated with the emitted electrons along with the spacecraft potential, and the lower panels (ic) and (iic) show the currents associated with the emitted ions.

magnetic field (Miyake et al. 2022), which is oriented predominantly antiparallel to the plasma flow. This appears to be notably enhanced compared to situations without SEE (Zhang et al. 2021a), due to the enhanced electron densities resulting from SEE. Due to this effect striking the inflowing boundary condition, the simulation box was expanded upstream as shown in Figure 1, up to the point where the wing structures no longer intersected the upstream plasma. This verified that this effect produced negligible (<1%) differences in the simulation results.

3.2. Secondary Emitted Currents

Figure 2 shows the current decomposition comparison for spacecraft at relatively low secondary emission density (ia–c) and at high secondary emission density (iia–c). These two scenarios represent two distinct regimes of Cassini charging to negative and positive potentials, as these simulations indicate occurs as Cassini descends into Saturn's ionosphere. The ultimate values reached in Figure 2 are therefore relevant to Cassini at Saturn, while the time history reveals the time-dependent interactions between the currents as the simulations reach steady state. The most interesting result is that there is significant reabsorption of the emitted electrons back onto the spacecraft. In Figure 2(iib), where the spacecraft is charging to a significant positive potential, over 50% of the emitted secondary electrons are reabsorbed back onto the spacecraft later, resulting in the net yield of the SEE emission being less than 40% of the neutral yield one would expect. Even in the

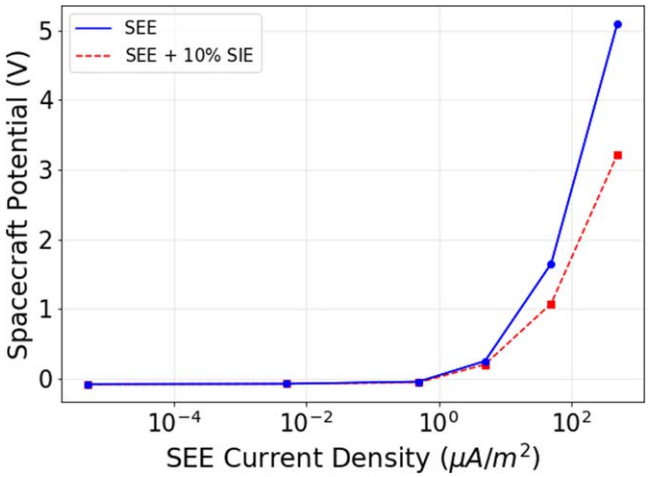

Figure 3. Spacecraft potential dependence upon the secondary electron emission current density (yield) with zero ion emission (blue) and where the ion emission is 10% of the electron emission (red).

case where there is little emission and the potential is negative, there is still significant reabsorption of the SEE electrons, due to the space-charge-limited effect, i.e., the Child–Langmuir law. This makes the net effect of the SEE current environment dependent, as well as a diminishing return of SEE density when the spacecraft becomes significantly positive, as can be seen in the later figures. The ions are, however, absorbed onto the spacecraft in much lower amounts, due to their larger emitted energies and greater momenta.

For the high-emission case, even though a majority of the SEE electrons are being reabsorbed, due to its high density it still dominates the positive currents in the system, as its "net" current is still much larger than the positive ion currents in the system. As a result, the spacecraft's current balance and hence its potential are controlled largely by the properties of the SEE currents.

In contrast, for the low-emission case, as shown in Figure 2(ib), because the density is much smaller, the "net" SEE current is now much smaller and the positive ion current becomes the significant current in the system, hence in this case the spacecraft would not be sensitive to the properties of the SEE currents.

3.3. Varying the Secondary Emission

Figure 3 shows the overall potential changes when one varies the secondary electron and ion emission currents in Equation (2). When the emission density is low ($<0.1\ \mu\mathrm{A\ m^{-2}}$), as expected at the top of the ionosphere, the potential of the spacecraft is virtually unchanged compared to when the secondary electrons and ions are not emitted. On the other hand, when the emission is high, as expected for higher neutral densities lower in the ionosphere, the spacecraft potential becomes very sensitive to the emitted currents, and not only do they successfully bring the spacecraft potential to positive values, they are able to raise its potential to up to >3 V at $500\mu\mathrm{A\ m^{-2}}$ SEE current density. This shows that secondary currents, with SEE in excess of SIE, are indeed able to raise the spacecraft potential significantly, thus achieving some of the same global effect on the spacecraft as dust currents.

We now compare our spacecraft potential results to Cassini measurements. In the absence of SEE and SIE, the simulated spacecraft potential is close to zero (-0.08 V) for the environmental conditions considered, as indeed is anticipated for an object moving through a cool, dense ionosphere. This baseline potential is dependent upon the electron temperature; if a temperature three times higher is used, a starting negative potential of -0.46 V will be obtained. This value is quite similar to the potential obtained in Zhang et al. (2021a), where the same temperature but with dust included obtained a potential of -0.42 V. Cassini at this altitude measured at -0.12 V, close to the simulated environment with a cold plasma.

The variation in secondary emission density, as shown in Figure 3, therefore represents a clear departure for the potentials, with clear dependence between the spacecraft potential and the neutral density, albeit mediated by the unknowns in the quantum yields. Using estimated yields and densities outlined in Section 2, Cassini is estimated to experience $\approx 5\ \mu\mathrm{A\ m^{-2}}$ of SEE and SIE at higher altitude (240 0 km) and $50\ \mu\mathrm{A\ m^{-2}}$ around the lowest altitude it experienced (1700 km). This corresponds to the range where SEE and SIE begin to make significant impacts on the potential of Cassini, as shown in Figure 3. Although there is much uncertainty surrounding these estimations, this illustrates the possibility of SIE and SEE becoming a factor in the positive spacecraft potential during Cassini's flybys. The spacecraft potentials reported by the Langmuir Probe (Morooka et al. 2019) show variations from just below -1 to $+0.6$ V, using an estimate from the maximum derivative of the current onto the probe. Johansson et al. (2022), however, suggest that the additional consideration of SEE changes the sweep interpretation and identifies higher potentials by determining the change between exponential and linear regions of the electron current in the current-voltage sweeps. The simulations presented herein therefore present constraints on the underlying system state, which can inform the various methods of inferring the spacecraft potential.

3.4. Emitted Electron Temperature

As electron emission is anticipated to dominate over ion emission, further attention is given to the properties of the emitted electrons. The temperature of the emitted electrons was implemented at 2 eV, as anticipated by Schmidt & Arends (1985), but this might well be be different for the interaction of Cassini's surface with Saturn's ionosphere, and Johansson et al. (2022) indeed indicate a lower temperature of 0.5 eV. Figure 4 therefore shows the sensitivity of the SEE current simulated under high- and low-emission current densities by varying the secondary electron's temperature. When the SEE current's magnitude is low, varying the temperature of the SEE species has almost no impact on the potential value of the spacecraft, and the spacecraft potential does not become positive. This is an expected result as, when the floating potential is negative, the electrons are strongly repelled and the emitted current density remains constant. However, for the much higher $50\ \mu\mathrm{A\ m^{-2}}$ current density case, by raising the temperature of the electrons by a factor of 10, the potential of the spacecraft raised from 1.6 V to almost 2.5 V. This trend supports the analysis of Figure 2 by showing that, the higher the current density of the SEE electrons, the more sensitive the spacecraft's potential is to the emitted electron temperature. This therefore shows that, when the spacecraft potential becomes positive, the characteristics of SEE might better provide an indicator of the characteristics of the neutrals striking the spacecraft.

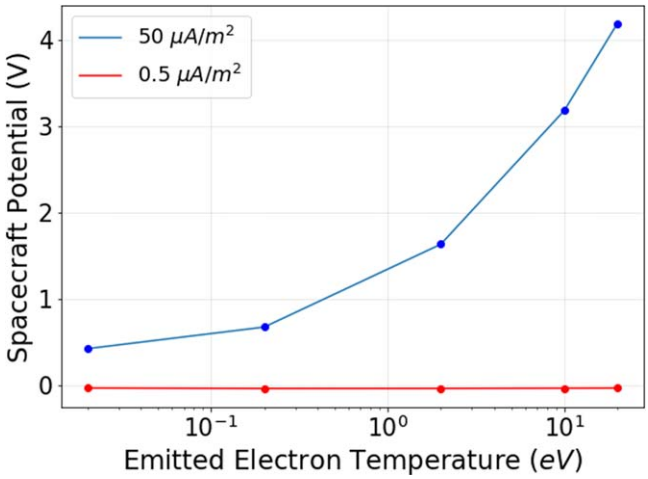

Figure 4. Spacecraft potential dependence upon temperature of the emitted electrons.

The secondary electron emission temperature inferred by Johansson et al. (2022) is 0.5 eV, notably lower than the laboratory-derived rates of Schmidt & Arends (1985). The variation of the SEE temperature in Figure 4 covers the temperature inferred by Johansson et al. (2022) under its varying range. The resultant trend showed that the spacecraft potential varies smoothly with emitted electron temperature when positively charged, and the spacecraft stays positively charged for large emission rates even at very low temperatures of 0.01 eV. Therefore, a sufficient emitted electron current would theoretically drive the Cassini spacecraft to positive potentials in Saturn's ionosphere, as inferred by Johansson et al. (2022). This variation with temperature also allows these results to be applicable to future missions where the environment and emitted electron characteristics could be different.

4. Discussion and Conclusions

In conclusion, we use three-dimensional PIC simulations to demonstrate that SEE theoretically represents a phenomenon for producing positive spacecraft potentials in Saturn's ionosphere. Specifically, when the amount of SEE is large ($>1\ \mu A\, m^{-2}$), spacecraft potentials were very sensitive to the SEE yield and hence the simulations could produce a smooth transition from negative to positive values as observed during the Grand Finale flybys (Morooka et al. 2019; Johansson et al. 2022). For small SEE and SIE yields, however, SEE and SIE induced negligible effects on the simulated Cassini spacecraft's plasma interaction.

The simulations show the emitted electrons propagate upstream of the spacecraft along the magnetic field and can then be reabsorbed, which means they might also be detected by the Langmuir Probe and other plasma instruments for specific spacecraft–magnetic field orientations. Figure 1 highlights how measurements of the ionospheric electrons might also be affected by the production of secondary electron populations. Identifying these reabsorbed electrons could also be useful for identifying SEE populations by other instruments on board Cassini, and they could help to calibrate for Langmuir Probe analysis of the ionospheric content.

The inference of charged dust populations in Saturn's equatorial ionosphere (Wahlund et al. 2018; Morooka et al. 2019) and the charge depletion of electrons of over 90% is consistent with Langmuir Probe observation at Enceladus (Wahlund et al. 2009; Morooka et al. 2011) and Titan (Agren et al. 2012; Shebanits et al. 2016), where large negatively charged ions and dust had been detected using Cassini's Plasma Spectrometer (Coates et al. 2007, 2010; Desai et al. 2017; Wellbrock et al. 2019; Mihailescu et al. 2020). In Saturn's ionosphere, the presence of negatively charged ions and dust is explained through the accumulation of infalling ring particles (Hsu et al. 2018; Mitchell et al. 2018) that undergo electron impact ionization processes and reduced photodetachment (Desai et al. 2021). In a preceding study, Zhang et al. (2021a) thus showed that charged dust can also produce a positive spacecraft potential when the positive species are overall more mobile than the negative species, with electron depletions of over 90%. This study, however, shows this is potentially explained by the phenomenon of neutral-induced electron and ion emission with electron emission rates dominating over the ion emission rates.

The amount of dust outside of the ionosphere is constrained by CDA (Hsu et al. 2018), INCA/CHEMS (Mitchell et al. 2018), and RPWS (Wahlund et al. 2018), and the amount of dust that falls into the equatorial region ionosphere from above D-ring is estimated at around 10–100 cm^{-3} at 1500 km, as projected by models to lower altitudes. A major outstanding question therefore remains as to the fate of these inflowing dust populations. When considering only the spacecraft potential, the two effects of SEE and charged dust cannot be distinguished from one another, and it is possible that both contributed to the positive potential observed at Saturn.

A definitive question within the SEE debate is what emission yields to use for which neutral species incident upon Cassini, which highlights the urgent need for further laboratory studies thereof. Here, we used emission rates typical for metals and those closest to the conditions at hand (Schmidt & Arends 1985), but these are still not directly representative of Saturn's atmospheric neutrals impacting Cassini, as they were designed for the 70 $km\, s^{-1}$ flybys of the Giotto and Vega missions (Grard & Mikhailov 1989), a velocity significantly higher than Cassini's 35 $km\, s^{-1}$. In this study, we also only considered water molecule densities derived from the ionospheric model of (Moore et al. 2018, Figure 2 therein). Observations from the Grand Finale revealed significant populations of methane, ammonia, and organics, in addition to the anticipated molecular hydrogen, helium, and water (Hsu et al. 2018; Mitchell et al. 2018; Waite et al. 2018), as well as NH_3, CO_2, CH_4, and the detections at 28 u, all having densities the same or higher as H_2O. These should all have energies sufficient to trigger electron emission from Cassini, as their energies in the spacecraft frame are expected to exceed the work function of the target surfaces. If these species have similar yields, the SEE current densities should be several factors—if not an order of magnitude—higher, which seems unphysically large. Such elevated SEE currents would drive Cassini to even higher potentials, but as the potential exceeds the peak of the Maxwellian of the emitted electron energies, fewer and fewer would be able to escape the potential well surrounding the spacecraft (Marchand et al. 2014). The emitted ions would, however, easily escape due to electrostatic repulsion. In this scenario, the positive charging would be

mediated by the SIE currents, which act to prevent the potential from diverging to extreme positive potentials.

A more accurate Cassini spacecraft model could also be used within further studies. For example, while the spacecraft is generally designed to be conducting, the high-gain antenna is coated in a resistive paint, the properties of which are not included herein. The most important factor for the plasma interaction is, however, the ram-pointing side of Cassini, and so for the first Grand Finale flyby, where Cassini flew with the HGA in ram, this effect would be most important. Given the uncertainties in the measurements of Saturn's ionospheric plasmas and the multitude of parameters that might therefore be varied, we have therefore opted to sweep through the most important parameters of interest. We directly compared our potentials (Figures 3 and 4) and found potentials similar to those inferred for Cassini (Morooka et al. 2019; Johansson et al. 2022), and the simulations results and trends discovered are therefore applicable to studies of spacecraft charging in Saturn's ionosphere and in similar environments.

It is also worth noting that, if accurate quantum yields were determined from neutral molecules onto Cassini thermal Kapton blankets, the spacecraft potentials might also yield further information on the neutral composition of the giant planet's atmospheric densities as the remaining unknown in Equation (2). In future missions where dust effects are small, accurate quantum yields might therefore be used to infer information on neutral populations from the spacecraft potential and measured incident currents.

Acknowledgments

Z.Z. acknowledges funding from the Royal Astronomical Society. R.T.D. acknowledges an STFC Ernest Rutherford Fellowship ST/W004801/1 and NERC grants NE/P017347/1 and NE/V003062/1. Y.M. and H.U. acknowledge grant No. 20K04041 from the Japan Society for the Promotion of Science (JSPS) and support from the innovative High Performance Computing Infrastructure (HPCI: hp210159) in Japan. O.S. acknowledges SNSA grant No. Dnr:195/20. F.L.J. acknowledges a grant from Lennanders stifelse. This work used the Imperial College High Performance Computing Service (doi:10.14469/hpc/2232).

Data Availability

All simulation data presented in this study can be retrieved from the Zenodo open-access repository at doi:10.5281/zenodo.4592954 (Zhang et al. 2021b).

ORCID iDs

Z. Zhang https://orcid.org/0000-0002-5672-2681
R. T. Desai https://orcid.org/0000-0002-2015-4053
O. Shebanits https://orcid.org/0000-0001-9621-211X
F. L. Johansson https://orcid.org/0000-0002-5386-8255
Y. Miyake https://orcid.org/0000-0001-6491-1012
H. Usui https://orcid.org/0000-0001-5846-9109

References

Agren, K., Edberg, N. J. T., & Wahlund, J. E. 2012, GeoRL, 39, L10201
Coates, A. J., Jones, G. H., Lewis, G. R., et al. 2010, Icar, 206, 618
Connerney, J. E. P., & Waite, J. H. 1984, Natur, 312, 136
Cravens, T. E., Moore, L., Waite, J. H., et al. 2019, GeoRL, 46, 6315
Coates, A. J., Crary, F. J., Lewis, G. R., et al. 2007, GeoRL, 34, L22103
Desai, R. T., Coates, A. J., Wellbrock, A., et al. 2017, ApJL, 844, L18
Desai, R. T., Zhang, Z., Wu, X., & Lue, C. 2021, PSJ, 2, 99
Dougherty, M. K., Cao, H., Khurana, K. K., et al. 2018, Sci, 362, aat5434
Grard, Pedersen, & Mikhailov, T. 1989, AnGeo, 7, 141
Hadid, L. Z., Morooka, M. W., Wahlund, J. E., et al. 2019, GeoRL, 46, 9362
Hsu, H.-W., Schmidt, J., Kempf, S., et al. 2018, Sci, 362, aat3185
Ip, W. H., Liu, C. M., & Pan, K. C. 2016, Icar, 276, 163
Johansson, F., Vigren, E., Waite, J. H., et al. 2022, MNRAS, 515, 2340
Kishinevsky, L. M. 1973, RadEf, 19, 23
Lamy, L., Zarka, P., Cecconi, B., et al. 2018, Sci, 362, aat2027
Lin, E. I., & Stultz, J. W. 1995, JTHT, 9, 778
Marchand, R., Miyake, Y., Usui, H., et al. 2014, PhPl, 21, 062901
Mihailescu, T., Desai, R. T., Shebanits, O., et al. 2020, PSJ, 1, 50
Mitchell, D. G., Perry, M. E., Hamilton, D. C., et al. 2018, Sci, 362, aat2236
Miyake, Y., Miloch, W. J., Kjus, S. H., & Pécseli, H. L. 2022, JGRA, 125, e27379
Miyake, Y., & Usui, H. 2009, PhPl, 16, 062904
Moore, L., Cravens, T. E., Müller-Wodarg, I., et al. 2018, GeoRL, 45, 9398
Moore, L., Galand, M., Mueller-Wodarg, I., Yelle, R., & Mendillo, M. 2008, JGRA, 113, A10306
Morooka, M. W., Wahlund, J. E., Eriksson, A. I., et al. 2011, JGRA, 116, A12221
Morooka, M. W., Wahlund, J. E., Hadid, L. Z., et al. 2019, JGRA, 124, 1679
Müller-Wodarg, I. C. F., Koskinen, T. T., Moore, L., et al. 2019, GeoRL, 46, 2372
Northrop, T. G., & Hill, J. R. 1982, JGR, 87, 6045
Roussos, E., Kollmann, P., Krupp, N., et al. 2018, Sci, 362, aat1962
Schmidt, R., & Arends, H. 1985, P&SS, 33, 667
Shebanits, O., Hadid, L. Z., Cao, H., et al. 2020, NatSR, 10, 7932
Shebanits, O., Wahlund, J.-E., Edberg, N. J. T., et al. 2016, JGRA, 121, 10
Sternglass, E. J. 1957, PhRv, 108, 1
Wahlund, J. E., André, M., Eriksson, A. I. E., et al. 2009, P&SS, 57, 1795
Wahlund, J. E., Morooka, M. W., Hadid, L. Z., et al. 2018, Sci, 359, 66
Waite, J. H., Perryman, R. S., Perry, M. E., et al. 2018, Sci, 362, aat2382
Wellbrock, A., Coates, A. J., Jones, G. H., et al. 2019, MNRAS, 490, 2254
Yelle, R. V., Serigano, J., Koskinen, T. T., et al. 2018, GeoRL, 45, 951
Young, D. T., Berthelier, J. J., Blanc, M., et al. 2004, SSRv, 114, 1
Zhang, Z., Desai, R. T., Miyake, Y., Usui, H., & Shebanits, O. 2021a, MNRAS, 504, 964
Zhang, Z., Desai, R. T., Miyake, Y., Usui, H., & Shebanits, M. 2021b, PIC simulation data of Cassini during the grand finale, Zenodo, doi:10.5281/zenodo.4592954